The Journal of Chemical Physics

Comparison between longitudinal viscoelastic relaxation and sound dispersion of molecular liquids on the molecular scale

Cite as: J. Chem. Phys. **156**, 244505 (2022); https://doi.org/10.1063/5.0098098
Submitted: 05 May 2022 • Accepted: 05 June 2022 • Accepted Manuscript Online: 06 June 2022 • Published Online: 29 June 2022

Tsuyoshi Yamaguchi

The Journal of Chemical Physics ARTICLE scitation.org/journal/jcp

Comparison between longitudinal viscoelastic relaxation and sound dispersion of molecular liquids on the molecular scale

Cite as: J. Chem. Phys. 156, 244505 (2022); doi: 10.1063/5.0098098
Submitted: 5 May 2022 • Accepted: 5 June 2022 •
Published Online: 29 June 2022

Tsuyoshi Yamaguchi[a)]

AFFILIATIONS

Graduate School of Engineering, Nagoya University, Chikusa, Nagoya 464-8603, Japan

[a)]Author to whom correspondence should be addressed: yamaguchi.tsuyoshi@material.nagoya-u.ac.jp

ABSTRACT

Molecular dynamics simulation on some molecular liquids was performed to study sound dispersion on the molecular scale. The sound velocity was determined from the intermediate scattering function, and the relation between the longitudinal modulus and frequency was compared with the frequency-dependent longitudinal modulus in the $q = 0$ limit evaluated by the Kubo–Green theory. The sound dispersion of a monoatomic liquid up to $q\sigma \cong 2$ was almost quantitatively explained by the viscoelasticity in the $q = 0$ limit when the wavenumber dependence of the heat capacity ratio was taken into account. The situation was similar for a polyatomic molecular liquid for which the intramolecular degrees of freedom were fixed. For a polyatomic liquid with intramolecular degrees of freedom, the sound dispersion on the molecular scale was connected to the high-frequency limit of the ultrasonic relaxation mode assigned to the vibrational energy relaxation. After subtracting the contribution of the vibrational energy relaxation, both the longitudinal viscoelasticity and the sound dispersion depended little on the presence of intramolecular degrees of freedom.

I. INTRODUCTION

Ultrasonic spectroscopy is one of the experimental methods for monitoring relaxation processes in liquids.[1] It measures the velocity or the attenuation coefficient of sound as a function of frequency. Simple hydrodynamics predicts sound velocity to be independent of frequency and the attenuation coefficient to be proportional to frequency squared, which actually holds in frequency ranges where no microscopic relaxation occurs. In other words, the microscopic relaxation processes can be observed as the deviation from the hydrodynamic frequency dependence.

Classical ultrasonic experiments using electric or optical devices have been performed in the frequency range below several GHz. Because the sound wavelength in this frequency range is much longer than the molecular size, the wavenumber dependence of material properties can be neglected, and the focus can be solely on frequency dependence.

Sound measurement at higher frequencies is possible by means of scattering experiments of quantum beams of shorter wavelengths. Traditionally, such experiments have been performed using thermal neutrons, and the Brillouin scattering experiments using x-ray or deep ultraviolet light are possible at the present time owing to the development of synchrotron facilities. The sound velocity in the THz frequency range, corresponding to the nm^{-1} wavenumber range, can be determined with these techniques, and experimental results on various liquids have been accumulated.[2–8]

On the molecular scale, the sound velocity is usually faster than that in the low-wavenumber limit, and it is often referred to as "fast sound."[2,9] The fast sound is sometimes ascribed to the viscoelastic relaxation of liquids, i.e., the sound velocity in the THz regime becomes higher because the structural relaxation is frozen. However, considering that the sound wavelength is comparable to the molecular size, the viscoelastic properties of a liquid may depend on the wavenumber in addition to frequency, and the effects of wavenumber and frequency are not separated. In molecular dynamics (MD) simulation, the sound velocity of a finite wavenumber can be evaluated from the intermediate scattering function. The viscoelastic relaxation in the zero-wavenumber ($q = 0$) limit can, in turn, be

determined from the time correlation functions associated with the stress tensor of the whole system through the Kubo–Green theory.[10] By comparing these two properties, we can evaluate how well the viscoelastic relaxation in the frequency regime can explain the sound dispersion in the molecular scale quantitatively, which is one of the principal purposes of this work.

The MD simulations and theoretical studies on fast sound have been performed mainly on simple monoatomic fluids and water, and the presence of the fast sound was successfully reproduced in these studies.[11–17] Upon extending the physical insights obtained on these two systems to polyatomic organic liquids, there are numerous additional factors that should be taken into account. For example, in a polyatomic organic molecule, the densities of mass and scattering length are delocalized. The repulsive core of an organic molecule is highly anisotropic, which leads to a strong coupling between the translational and rotational modes. In classical ultrasonic studies, it is also well known that the presence of the intramolecular vibrational modes can be a reason for sound dispersion through vibrational energy relaxation.[18,19] The second purpose of this work is to examine the effects of these factors that are specific to polyatomic liquids.

To increase the complexity of the system step by step in this work, three target systems were chosen. The first one is a monoatomic Lennard-Jones (LJ) fluid, which is considered as the starting point of our computational analysis. The results of our MD simulation are analyzed based on the well-established theory on the acoustic wave of a simple fluid. The second system is liquid cyclohexane, the intramolecular geometry of which was fixed to the stable chair conformation. The theory on a simple liquid is extended there and used for analysis. The third system is liquid cyclohexane, the intramolecular degrees of freedom of which are included. Particular attention was devoted here to the coupling of vibrational energy relaxation with longitudinal viscoelasticity, and a novel theoretical method is proposed for analyzing the contributions of the vibrational energy relaxation. We would like to comment here that the latter two models of cyclohexane were chosen to clarify the contributions of various factors specific to polyatomic molecular liquids, and we do not intend to reproduce the acoustic properties of real cyclohexane liquid in this work.

This paper is organized as follows: Sec. II gives the detailed description of the systems under consideration. The theoretical formulation is given in Sec. III, and Sec. IV is devoted to the computational procedures. The numerical results are, then, shown in Sec. V, moving from the simpler to the more complex ones. The results of all the systems are, then, summarized in Sec. VI.

II. SYSTEMS UNDER CONSIDERATION

The first system considered in this study is the one-component LJ fluid. All the physical quantities of the LJ fluid are given in LJ reduced units, in which the LJ parameters ϵ (the depth of the interaction potential) and σ (atomic diameter), the mass of an atom m, and the Boltzmann constant k_B are unity. The numerical calculations were performed at two thermodynamic conditions. The temperature was set at $T = 0.75$ and 3.0, whereas the number density ρ was fixed at 0.85. The condition of $T = 0.75$ corresponds to the liquid close to the triple point, and $T = 3.0$ corresponds to the compressed gas above the critical temperature.

Second, we treat a model polyatomic liquid composed of rigid cyclohexane molecules described by the TraPPE-UA model.[20] In the TraPPE-UA model, the methylene ($-CH_2-$) group is treated as a united atom. The cyclohexane molecule in this model is, thus, a six-site cyclic molecule. The C–C bond lengths are fixed at 0.154 nm as determined in the TraPPE-UA model. The bond angles, which are usually treated as flexible, were also fixed at 114.0° by keeping the dihedral angles in the chair form. The temperature was 298.15 K, and the density was set to be the experimental value at ambient pressure.[21]

The third model liquid considered is the six-site united atom model of cyclohexane for which the intramolecular degrees of freedom are fully taken into account. The nonbonding interaction between two methylene sites was taken from the TraPPE-UA model. The potentials for the bond angle and the dihedral angle were also taken from the TraPPE-UA model. Although the bond lengths are fixed in the TraPPE-UA model, they are described by the harmonic potential for which the bottom and spring constant are 0.154 nm and 5.02416×10^5 kJ mol^{-1} nm^{-2}, respectively. In short, the third model cyclohexane is the same as the second one, except for the treatment of the intramolecular degrees of freedom.

Our focus of the third model is mainly on the contribution of the vibrational energy relaxation to sound dispersion, and we would like to comment here on two possible artifacts in this model. First, in principle, the intramolecular vibrational modes should be treated in a quantum way because its vibrational frequency is usually larger than that of the thermal energy, k_BT. The classical approximation overestimates the vibrational heat capacity, which results in an overestimation of the contribution of the vibrational energy relaxation to sound dispersion. The second artifact is the use of the united atom model for the methylene group, which neglects the intramolecular vibrational modes associated with hydrogen atoms. The neglect of these modes leads to an underestimation of the vibrational heat capacity, but we believe that its effect is small because vibrational excitations of these modes are in reality, suppressed in a quantum way.

III. THEORETICAL FORMULATION

A. Simple LJ fluid

The theory on the dynamics of simple fluids is already well-established, and the theoretical formulation below follows the textbook of Boon and Yip.[9]

The theory is based on the generalized Langevin formalism, where the degrees of freedom of the system are divided into slow and fast. The time development of the former is treated explicitly, whereas the contribution of the latter is regarded as a random force. The densities of conserved quantities are usually regarded as the set of the slow variables in considering the dynamics in low-q regime, where q stands for the wavenumber. The conserved quantities in the present system are the number of molecules, the linear momenta, and the total energy, and their corresponding densities are, respectively, defined in the reciprocal space as follows:

$$\tilde{\rho}_n(\boldsymbol{q}) \equiv \sum_l \exp(i\boldsymbol{q}\cdot\boldsymbol{r}_l), \tag{1}$$

$$\tilde{\boldsymbol{j}}_m(\boldsymbol{q}) \equiv \sum_l m\dot{\boldsymbol{r}}_l \exp(i\boldsymbol{q}\cdot\boldsymbol{r}_l), \tag{2}$$

$$\tilde{\rho}_\epsilon(\boldsymbol{q}) \equiv \sum_l \left[\frac{1}{2}m|\dot{\boldsymbol{r}}_l|^2 + \frac{1}{2}\sum_{l'} u(\boldsymbol{r}_{ll'})\right] \exp(i\boldsymbol{q}\cdot\boldsymbol{r}_l). \tag{3}$$

Here, the summation over l runs over all the atoms and that of l' does $l' \neq l$. The position of atom l is denoted as $\boldsymbol{r}_l$, $\boldsymbol{r}_{ll'}$ indicates the relative position between atoms l and l', and $u(\boldsymbol{r}_{ll'})$ stands for the potential function of the interaction energy between them. In homogeneous fluids, the quantities at different $\boldsymbol{q}$ values are decoupled from each other because of the translational symmetry. The momentum density $\tilde{\boldsymbol{j}}_m(\boldsymbol{q})$ was divided into longitudinal ($\tilde{\boldsymbol{j}}_m \parallel \boldsymbol{q}$) and transverse ($\tilde{\boldsymbol{j}}_m \perp \boldsymbol{q}$) components, and only the longitudinal component is coupled to the number density $\tilde{\rho}_n(\boldsymbol{q})$ and the energy density $\tilde{\rho}_\epsilon(\boldsymbol{q})$. Hereafter, we set the coordinate of the system such that the z axis is parallel to $\boldsymbol{q}$, and the magnitude of the vector $\boldsymbol{q}$ is denoted as q. The longitudinal momentum density is, thus, described as $\tilde{j}_{m,z}(\boldsymbol{q})$. Considering that $\tilde{\rho}_\epsilon(\boldsymbol{q})$ is not orthogonal to $\tilde{\rho}_n(\boldsymbol{q})$, a new variable is defined as

$$\tilde{\rho}_{\epsilon'}(\boldsymbol{q}) \equiv \tilde{\rho}_\epsilon(\boldsymbol{q}) - \frac{\langle\tilde{\rho}_n^*(\boldsymbol{q})\tilde{\rho}_\epsilon(\boldsymbol{q})\rangle}{\langle\tilde{\rho}_n^*(\boldsymbol{q})\tilde{\rho}_n(\boldsymbol{q})\rangle}\tilde{\rho}_n(\boldsymbol{q}), \tag{4}$$

which is orthogonal to both $\tilde{\rho}_n(\boldsymbol{q})$ and $\tilde{j}_{m,z}(\boldsymbol{q})$.

Based on the standard theoretical procedure, the time development of $\tilde{\rho}_n(\boldsymbol{q})$, $\tilde{j}_{m,z}(\boldsymbol{q})$, and $\tilde{\rho}_{\epsilon'}(\boldsymbol{q})$ is given by the generalized Langevin equation (GLE) as follows:

$$\dot{\tilde{\rho}}_n(\boldsymbol{q},t) = \frac{iq}{m}\tilde{j}_{m,z}(\boldsymbol{q},t), \tag{5}$$

$$\begin{aligned}\dot{\tilde{j}}_{m,z}(\boldsymbol{q},t) = &-\frac{iq}{m}\frac{\langle\tilde{j}_{m,z}^*(\boldsymbol{q})\tilde{j}_{m,z}(\boldsymbol{q})\rangle}{\langle\tilde{\rho}_n^*(\boldsymbol{q})\tilde{\rho}_n(\boldsymbol{q})\rangle}\tilde{\rho}_n(\boldsymbol{q},t)\\ &+\frac{\langle\tilde{\rho}_{\epsilon'}^*(\boldsymbol{q})\dot{\tilde{j}}_{m,z}(\boldsymbol{q})\rangle}{\langle\tilde{\rho}_{\epsilon'}^*(\boldsymbol{q})\tilde{\rho}_{\epsilon'}(\boldsymbol{q})\rangle}\tilde{\rho}_{\epsilon'}(\boldsymbol{q},t)\\ &-\int_0^t d\tau\tilde{K}_{jj}(\boldsymbol{q},t-\tau)\tilde{j}_{m,z}(\boldsymbol{q},\tau) + \tilde{R}_j(\boldsymbol{q},t),\end{aligned} \tag{6}$$

$$\begin{aligned}\dot{\tilde{\rho}}_{\epsilon'}(\boldsymbol{q},t) = &-\frac{\langle\tilde{\rho}_{\epsilon'}^*(\boldsymbol{q})\dot{\tilde{j}}_{m,z}(\boldsymbol{q})\rangle}{\langle\tilde{j}_{m,z}^*(\boldsymbol{q})\tilde{j}_{m,z}(\boldsymbol{q})\rangle}\tilde{j}_{m,z}(\boldsymbol{q},t)\\ &-\int_0^t d\tau\tilde{K}_{\epsilon'\epsilon'}(\boldsymbol{q},t-\tau)\tilde{\rho}_{\epsilon'}(\boldsymbol{q},t) + \tilde{R}_{\epsilon'}(\boldsymbol{q},t).\end{aligned} \tag{7}$$

The cross terms of the memory functions are neglected here due to the different symmetries of the random forces $\tilde{R}_j(\boldsymbol{q},t)$ and $\tilde{R}_{\epsilon'}(\boldsymbol{q},t)$ in the $q = 0$ limit.[9]

The comparison of the GLEs above with the hydrodynamic equations relates the memory functions $\tilde{K}_{jj}(\boldsymbol{q},t)$ and $\tilde{K}_{\epsilon'\epsilon'}(\boldsymbol{q},t)$ with the transport coefficients. The former $\tilde{K}_{jj}(\boldsymbol{q},t)$ is related to the frequency-dependent and wavenumber-dependent longitudinal viscosity, $\eta_L(\omega,q)$, as follows:

$$\frac{q^2}{\rho_m}\eta_L(\omega,q) = \int_0^\infty dt e^{-i\omega t}\tilde{K}_{jj}(\boldsymbol{q},t). \tag{8}$$

Here, the mass density is denoted as ρ_m and ω stands for angular frequency. The $q = 0$ limit, $\eta_L(\omega,\ q=0)$, is given by the linear combinations of the frequency-dependent shear and volume viscosities, denoted as $\eta_s(\omega)$ and $\eta_v(\omega)$, respectively, as follows:

$$\eta_L(\omega) \equiv \eta_L(\omega,\ q=0) = \eta_v(\omega) + \frac{4}{3}\eta_s(\omega). \tag{9}$$

The wavenumber-dependent heat diffusivity, $D_T(q)$, is related to $\tilde{K}_{\epsilon'\epsilon'}(\boldsymbol{q},t)$ as follows:

$$q^2 D_T(q) = \int_0^\infty dt\tilde{K}_{\epsilon'\epsilon'}(\boldsymbol{q},t). \tag{10}$$

The quantity directly determined in the Brillouin spectroscopy is the dynamic structure factor, the inverse Fourier transformation of which, with respect to frequency, gives the intermediate scattering function defined as

$$\tilde{I}(q,t) \equiv \frac{1}{V}\langle\tilde{\rho}_n^*(\boldsymbol{q},\ t=0)\tilde{\rho}_n(\boldsymbol{q},t)\rangle, \tag{11}$$

where V stands for the volume of the system. Its initial value, denoted as

$$\tilde{\chi}(q) \equiv \tilde{I}(q,\ t=0) = \frac{1}{V}\langle\tilde{\rho}_n^*(\boldsymbol{q})\tilde{\rho}_n(\boldsymbol{q})\rangle, \tag{12}$$

is the static structure factor.

The intermediate scattering function is in some cases described by the sum of the exponential decay and the damped oscillation as follows:[9,22]

$$\begin{aligned}\frac{\tilde{I}(q,t)}{\tilde{\chi}(q)} = &(1-a_P(q))\left[e^{-k_T(q)t} + \frac{k_T(q)}{\omega_P'(q)}e^{-k_P(q)t}\sin\omega_P'(q)t\right]\\ &+ a_P(q)e^{-k_P(q)t}\left[\cos\omega_P'(q)t + \frac{k_P(q)}{\omega_P'(q)}\sin\omega_P'(q)t\right].\end{aligned} \tag{13}$$

The first exponential term in the first square bracket gives the thermal diffusion (Rayleigh line), and the second square bracket is ascribed to the longitudinal acoustic wave (Brillouin doublet). The second terms in the square brackets are introduced to guarantee $\ddot{\tilde{I}}(q,t) = 0$. The wavenumber-dependent sound velocity, $c(q)$, is, then, given by

$$c^2(q)q^2 = \omega_P^2(q) \equiv \omega_P'^2(q) + k_P^2(q). \tag{14}$$

The relation between $\omega_P(q)$ and $c(q)$ gives the sound dispersion as a function of frequency.

From Eqs. (5) and (6), the low-frequency limiting value of the isothermal sound velocity, $c_{T,0}(q)$, is given at the limit of $\tilde{K}_{jj}(\boldsymbol{q},t) = 0$ and $\tilde{\rho}_{\epsilon'}(\boldsymbol{q},t) = 0$ as

$$c_{T,0}^2(q) = \frac{\langle\tilde{j}_{m,z}^*(\boldsymbol{q})\tilde{j}_{m,z}(\boldsymbol{q})\rangle}{m^2\langle\tilde{\rho}_n^*(\boldsymbol{q})\tilde{\rho}_n(\boldsymbol{q})\rangle}. \tag{15}$$

The adiabatic sound velocity in the low-frequency limit, $c_{S,0}(q)$, then, corresponds to the limit of $\tilde{K}_{jj}(\boldsymbol{q},t) = 0$ and $\tilde{K}_{\epsilon'\epsilon'}(\boldsymbol{q},t) = 0$ as

$$c_{S,0}^2(q) = c_{T,0}^2(q) + \frac{\left|\langle\tilde{\rho}_{\epsilon'}^*(\boldsymbol{q})\dot{\tilde{j}}_{m,z}(\boldsymbol{q})\rangle\right|^2}{q^2\langle\tilde{\rho}_{\epsilon'}^*(\boldsymbol{q})\tilde{\rho}_{\epsilon'}(\boldsymbol{q})\rangle\langle\tilde{j}_{m,z}^*(\boldsymbol{q})\tilde{j}_{m,z}(\boldsymbol{q})\rangle}, \tag{16}$$

and their ratio defines the wavenumber-dependent heat capacity ratio as

$$\gamma(q) \equiv \frac{c_{S,0}^2(q)}{c_{T,0}^2(q)}. \tag{17}$$

The high-frequency limiting values of the isothermal and adiabatic sound velocities, denoted as $c_{T,\infty}(q)$ and $c_{S,\infty}(q)$, respectively, are related to the second derivative of the longitudinal momentum correlation function as

$$c_{T,\infty}^2(q) = \frac{\left\langle \ddot{\tilde{j}}_{m,z}^*(\boldsymbol{q}) \ddot{\tilde{j}}_{m,z}(\boldsymbol{q}) \right\rangle}{q^2 \left\langle \tilde{j}_{m,z}^*(\boldsymbol{q}) \ddot{\tilde{j}}_{m,z}(\boldsymbol{q}) \right\rangle}, \tag{18}$$

$$c_{S,\infty}^2(q) = c_{T,\infty}^2(q) + c_{S,0}^2(q) - c_{T,0}^2(q). \tag{19}$$

When the memory functions $\tilde{K}_{jj}(\boldsymbol{q},t)$ and $\tilde{K}_{\epsilon'\epsilon'}(\boldsymbol{q},t)$ are Markovian, the damping coefficients $k_T(q)$ and $k_P(q)$ are related to the frequency-independent transport coefficients as

$$k_T(q) = D_T(q)q^2, \tag{20}$$

$$2k_P(q) = \left[\frac{\eta_L(q)}{\rho_m} + [\gamma(q) - 1] D_T(q) \right] q^2. \tag{21}$$

In the presence of slow relaxation modes in liquid, the memory function $\tilde{K}_{jj}(\boldsymbol{q},t)$ becomes non-Markovian, and the longitudinal viscosity is a complex function of frequency,

$$\eta_L(q,\omega) = \eta_L'(q,\omega) - \frac{i}{\omega}\Delta G_L'(q,\omega), \tag{22}$$

where the first and the second terms of the right-hand side denote the real and imaginary parts, respectively. In such a case, Eq. (13) is, in principle, unable to describe the intermediate scattering function in the whole-time region. However, when the frequency dependence of $\eta_L(q,\omega)$ is not strong, the description of the intermediate scattering function by Eq. (13) approximately holds, and the apparent sound velocity and damping coefficient are given by

$$c^2(q) \simeq c_{S,0}^2(q) + \frac{\Delta G_L'(q,\omega_P(q))}{\rho_m}, \tag{23}$$

$$2k_P(q) \simeq \left[\frac{\eta_L'(q,\omega_P(q))}{\rho_m} + [\gamma(q) - 1] D_T(q) \right] q^2. \tag{24}$$

With these equations, the longitudinal viscoelastic relaxation, $\eta_L(q,\omega)$, can be determined from the acoustic wave in the intermediate scattering function.

The longitudinal viscosity in the hydrodynamic limit is related to the volume viscosity and the shear viscosity. According to the Kubo–Green theory, the shear viscosity is, in turn, given by the time correlation function of the pressure tensor as[10]

$$\eta_s(\omega) = \int_0^\infty dt e^{-i\omega t} G(t), \tag{25}$$

$$G(t) \equiv \frac{V}{k_B T} \langle P_{xz}(0) P_{xz}(t) \rangle, \tag{26}$$

where k_B and T stand for the Boltzmann constant and the absolute temperature, respectively. The Kubo–Green theory also describes the volume viscosity in terms of the time correlation function of the adiabatic pressure fluctuation, $\delta P'(t)$, as follows:[23–26]

$$\eta_v(\omega) = \int_0^\infty dt e^{-i\omega t} K(t), \tag{27}$$

$$K(t) \equiv \frac{V}{k_B T} \langle \delta P'(0) \delta P'(t) \rangle. \tag{28}$$

When calculating $K(t)$ by means of MD simulation, the expression of $\delta P'(t)$ changes according to the ensemble of the system. In a constant-volume constant-temperature (NVT) ensemble, which was used in this work, the effect of the total energy variation, $\delta E(t)$, should be linearly projected out from the pressure fluctuation, $\delta P(t)$, as follows:

$$\delta P'(t) \equiv \delta P(t) - \frac{\langle \delta P \delta E \rangle}{\langle |\delta E|^2 \rangle} \delta E(t). \tag{29}$$

B. Extension to rigid molecular liquid

The dynamics of polyatomic molecular liquids described in this study is based on the interaction-site model, where the rotation of rigid molecules is described as a coupled translation of interaction sites.[27] Given that the number density of each site is a conserved quantity, these number density modes behave as slow modes, to be treated as explicit variables in a GLE formalism, and the intermediate scattering function becomes a square matrix with the dimension equal to the number of sites. In the present cyclohexane model, however, only the total number density of the methylene sites is relevant in the consideration of Brillouin spectroscopy because all six sites are equivalent and other five components are decoupled from the total number density mode. Therefore, $\tilde{\rho}_n(\boldsymbol{q})$ is defined for model cyclohexane as the total number density of the interaction sites as follows:

$$\tilde{\rho}_n(\boldsymbol{q}) \equiv \sum_l \sum_{\alpha \in l} \exp(i\boldsymbol{q} \cdot \boldsymbol{r}_{l\alpha}). \tag{30}$$

The index l runs over whole *molecules*, and α refers to the interaction site that belongs to molecule l. The scattering length of all the sites is equal, and thus, the scattering length density is proportional to $\tilde{\rho}_n(\boldsymbol{q})$, and the inelastic scattering spectrum is given as the Fourier transformation of the autocorrelation function of $\tilde{\rho}_n(\boldsymbol{q})$, which is denoted as $\tilde{I}(q,t)$ and is defined by substituting $\tilde{\rho}_n(\boldsymbol{q})$ defined by Eq. (30) into Eq. (12). The definition of the momentum density is also modified as

$$\tilde{\boldsymbol{j}}_m(\boldsymbol{q}) \equiv \sum_l \sum_{\alpha \in l} m \dot{\boldsymbol{r}}_{l\alpha} \exp(i\boldsymbol{q} \cdot \boldsymbol{r}_{l\alpha}), \tag{31}$$

where m stands for the mass of the CH_2 site for our model cyclohexane. The energy density is, then, given by

$$\tilde{\rho}_\epsilon(\boldsymbol{q}) \equiv \sum_l \sum_{\alpha \in l} \left[\frac{1}{2} m |\dot{\boldsymbol{r}}_{l\alpha}|^2 + \frac{1}{2} \sum_{l'} \sum_{\alpha'} u(\boldsymbol{r}_{l\alpha,l'\alpha'}) \right] \exp(i\boldsymbol{q} \cdot \boldsymbol{r}_{l\alpha}). \tag{32}$$

The summation of the kinetic energies of sites within a molecule is equal to the sum of the translational and rotational energies of the molecule. The rotational energy is, thus, implicitly included in the first term of the square bracket. With these modifications of the definitions of variables, the theoretical formulation for simple fluid is applicable to the polyatomic liquids composed of rigid molecules.

We shall here comment on the effects of the site asymmetry of the molecule. Owing to the equivalence of the six sites of this model cyclohexane, the densities of both mass and scattering length are proportional to $\tilde{\rho}_n(\boldsymbol{q})$, and the contributions of other five components of the site densities, which are associated with the rotational modes, can be neglected. When the sites within the molecule are heterogeneous, the intermediate scattering function $\tilde{I}(q,t)$ becomes different from the time correlation function of $\tilde{\rho}_n(\boldsymbol{q})$, and the time derivative of $\tilde{\rho}_n(\boldsymbol{q})$ is not proportional to $\tilde{\boldsymbol{j}}_m(\boldsymbol{q})$. Even in such a case, the contribution of the rotational mode can be neglected in the small q regime because it is proportional to q^2 in the low-q limit. The effects of the coupling with the rotational modes, then, increase with increasing q, which can be a reason for the discrepancy between the longitudinal viscoelasticity determined by the sound dispersion at a finite wavenumber and that of the $q = 0$ limit.

C. Treatment of intramolecular vibration

The description of the dynamics based on the interaction-site model is also used for the third model, and the definitions of the number density and the momentum density are the same as that for the rigid model, Eqs. (30) and (31). The energy density, $\tilde{\rho}_\epsilon(\boldsymbol{q})$, should be modified to include the intramolecular vibrational energy.

The rigid and the intramolecular parts of the energy density, denoted as $\tilde{\rho}_{\epsilon 1}(\boldsymbol{q})$ and $\tilde{\rho}_{\epsilon 2}(\boldsymbol{q})$, respectively, are defined first as below. The definition requires the division of the kinetic energy, which begins with that of the site velocity, $\dot{\boldsymbol{r}}_{l\alpha}$, into three terms as follows:

$$\dot{\boldsymbol{r}}_{l\alpha} = \boldsymbol{v}_{CM,l} + \boldsymbol{v}_{R,l\alpha} + \boldsymbol{v}_{I,l\alpha}. \tag{33}$$

The first term stands for the center-of-mass velocity of the molecule l with a usual definition. The second term denotes the rotational velocity, and the remaining part is assigned to the intramolecular velocity, $\boldsymbol{v}_{I,l\alpha}$. The definition of the rotational velocity, $\boldsymbol{v}_{R,l\alpha}$, is given by

$$\boldsymbol{v}_{R,l\alpha} \equiv \boldsymbol{\omega}_l \times \boldsymbol{\delta r}_{l\alpha}, \tag{34}$$

$$\boldsymbol{\omega}_l \equiv \boldsymbol{I}_l^{-1} \cdot \sum_\alpha (\boldsymbol{\delta r}_{l\alpha} \times m\dot{\boldsymbol{r}}_{l\alpha}), \tag{35}$$

where $\boldsymbol{I}_l$ stands for the inertia moment tensor and $\boldsymbol{\delta r}_{l\alpha}$ denotes the relative position of site α in the molecule l from the molecular center-of-mass. Even if a molecule can take various conformations, such as chair and boat forms of cyclohexane, the translational and the rotational velocities are defined in the same way by evaluating the inertia moment tensor using the instantaneous conformation of the molecule. With these definitions of velocities, $\tilde{\rho}_{\epsilon 1}(\boldsymbol{q})$ and $\tilde{\rho}_{\epsilon 2}(\boldsymbol{q})$ are defined as

$$\tilde{\rho}_{\epsilon 1}(\boldsymbol{q}) \equiv \sum_l \sum_{\alpha \in l} \left[\frac{1}{2} m |\boldsymbol{v}_{CM,l} + \boldsymbol{v}_{R,l\alpha}|^2 + \frac{1}{2} \sum_{l'} \sum_{\alpha'} u(\boldsymbol{r}_{l\alpha,l'\alpha'}) \right] \times \exp(i\boldsymbol{q} \cdot \boldsymbol{r}_{l\alpha}), \tag{36}$$

$$\tilde{\rho}_{\epsilon 2}(\boldsymbol{q}) \equiv \sum_l \sum_{\alpha \in l} \left[\frac{1}{2} m |\boldsymbol{v}_{I,l\alpha}|^2 + \varphi_{l\alpha} \right] \exp(i\boldsymbol{q} \cdot \boldsymbol{r}_{l\alpha}). \tag{37}$$

Here, the intramolecular vibrational potential energy of a molecule l is divided into the contributions of site α as the second term of the square bracket of Eq. (37), $\varphi_{l\alpha}$. The definition of $\varphi_{l\alpha}$ is somewhat arbitrary, and the following convention was used in the numerical calculation in this study. The bond stretching energy is equally assigned to the two sites connected by the bond. The potential energy associated with the bond angle is wholly assigned to the central site. The A–B–C–D dihedral potential was equally assigned to the central two sites, B and C. Although in the present model the intramolecular LJ and electrostatic interactions are absent, they should be included in $\varphi_{l\alpha}$ if present. In the case of the rigid model, the definition of $\tilde{\rho}_{\epsilon 1}(\boldsymbol{q})$ by Eq. (36) is equal to that of $\tilde{\rho}_\epsilon(\boldsymbol{q})$ by Eq. (32) because $\boldsymbol{v}_{I,l\alpha}$ in Eq. (33) is equal to zero.

The summation of $\tilde{\rho}_{\epsilon 1}(\boldsymbol{q})$ and $\tilde{\rho}_{\epsilon 2}(\boldsymbol{q})$ gives the total energy density as

$$\tilde{\rho}_\epsilon(\boldsymbol{q}) = \tilde{\rho}_{\epsilon 1}(\boldsymbol{q}) + \tilde{\rho}_{\epsilon 2}(\boldsymbol{q}), \tag{38}$$

which is explicitly given by

$$\tilde{\rho}_\epsilon(\boldsymbol{q}) = \sum_l \sum_{\alpha \in l} \left[\frac{1}{2} m \left\{ |\boldsymbol{v}_{CM,l} + \boldsymbol{v}_{R,l\alpha}|^2 + |\boldsymbol{v}_{I,l\alpha}|^2 \right\} + \frac{1}{2} \sum_{l'} \sum_{\alpha'} u(\boldsymbol{r}_{l\alpha,l'\alpha'}) + \varphi_{l\alpha} \right] \exp(i\boldsymbol{q} \cdot \boldsymbol{r}_{l\alpha}). \tag{39}$$

The kinetic energy term in Eq. (39) is different from the ordinary one, $\frac{1}{2} m |\dot{\boldsymbol{r}}_{l\alpha}|^2$. Provided that the difference in the two definitions of the kinetic energy disappears after the summation over all the sites within a molecule, the difference can be regarded like the difference in the division of the kinetic energy of a molecule into the contributions of its sites.

The exclusion of the linear correlations with the number density mode, $\tilde{\rho}_n(\boldsymbol{q})$, defines $\tilde{\rho}_{\epsilon 1'}(\boldsymbol{q})$ and $\tilde{\rho}_{\epsilon 2'}(\boldsymbol{q})$, respectively [Eq. (4)]. Note that $\tilde{\rho}_{\epsilon 1'}(\boldsymbol{q})$ and $\tilde{\rho}_{\epsilon 2'}(\boldsymbol{q})$ might not be orthogonal to each other.

The fluctuation of the total energy, $\delta E(t)$ in Eq. (29), can also be divided into a rigid and an intramolecular part, denoted as $\delta E_1(t)$ and $\delta E_2(t)$, respectively. Their definition is omitted here for brevity because they are similar to Eqs. (36) and (37). The exchange of energy between $\delta E_1(t)$ and $\delta E_2(t)$ corresponds to the vibrational energy relaxation. The linear correlation with δE is, then, excluded to define $\delta E_1'$ and $\delta E_2'$ as performed on δP in Eq. (29). We propose here the division of $\eta_v(\omega)$ into a rigid and an intramolecular part, denoted as $\eta_{v1}(\omega)$ and $\eta_{v2}(\omega)$, respectively, based on the division of the total energy fluctuation.

First, we rewrite the Kubo–Green formula for $\eta_v(\omega)$ [Eqs. (27) and (28)] using the Liouvillian operator, L, as follows:

$$\eta_v(\omega) = \frac{V}{k_B T} \int_0^\infty dt e^{-i\omega t} \left\langle \delta P' e^{iLt} \delta P' \right\rangle. \tag{40}$$

Next, the projection operator onto $\delta E_2'(t)$ is denoted as P_2, and the projection operator Q_2 is defined as $Q_2 = 1 - P_2$. The rigid part of the volume viscosity, $\eta_{v1}(\omega)$, is connected to the time correlation function of the projected Liouvillian, $Q_2 L Q_2$, as

$$\eta_{v1}(\omega) = \eta_v(\omega) - \eta_{v2}(\omega) = \frac{V}{k_B T}\int_0^\infty dt e^{-i\omega t}\left\langle \delta P' e^{iQ_2 L Q_2 t} Q_2 \delta P' \right\rangle \quad (41)$$

because it means that the viscoelastic relaxation under the condition that the intramolecular vibrational energy is frozen. After some mathematical calculations, which is described in Sec. S1 of the supplementary material in detail, the expression of the intramolecular part, $\eta_{v2}(\omega)$, is simply given as

$$\eta_{v2}(\omega) = \frac{V\left[\int_0^\infty dt e^{-i\omega t}\left\langle \delta P' e^{iLt}\delta E_2'\right\rangle\right]^2}{k_B T \int_0^\infty dt e^{-i\omega t}\left\langle \delta E_2' e^{iLt}\delta E_2'\right\rangle}, \quad (42)$$

and its direct evaluation is possible by MD simulation.

IV. COMPUTATIONAL DETAILS

All the simulation runs throughout this work were performed using the GROMACS software package.[28] All the molecules in a system were contained in a cubic cell with a periodic boundary condition. The volume of the cell was fixed, whereas the temperature was controlled by means of the Nosé–Hoover method.[29] The equation of motion was integrated using the leapfrog algorithm.

The MD simulation runs of the first model were performed on systems composed of 8000 LJ atoms. The time steps of the integration of the equation of motion were $\Delta t = 0.001$ for $T = 0.75$ and 0.0005 for $T = 3.0$. The duration of production runs was 10^8 steps for $T = 0.75$ and 5×10^7 steps for $T = 3.0$, respectively, and both runs were preceded by equilibration runs of more than 10^7 steps. The intermolecular LJ interaction was cut off at a distance of $r = 4.0$. The time constant of the Nosé–Hoover thermostat was chosen to be $\tau_{\mathrm{bath}} = 100$, which was considered to be sufficiently small to exclude possible artifacts due to the coupling with the thermostat.

The simulation run of the second model was performed on a system composed of 1210 cyclohexane molecules. The time constant of the bath was set at 100 ps, and the equation of motion was integrated with a time step of 1 fs. The intramolecular geometry was fixed using the SHAKE algorithm.[29] The duration of the production run was 100 ns, preceded by an equilibration run of 100 ns duration.

The conditions of the MD simulation runs of the flexible cyclohexane liquid were the same as for the rigid one, except for the absence of the constraints of intramolecular geometry. Because the Nosé–Hoover thermostat is also directly coupled to the kinetic part of the intramolecular vibrational energy, the presence of the thermostat may affect the rate of vibrational energy relaxation. We, thus, performed several runs with different values of the time constant of the bath and confirmed that the coupling was weak enough and the effect of the thermostat on the vibrational energy relaxation was negligible when the time constant was 100 ps.

V. RESULTS AND DISCUSSION

A. Simple atomic fluids

The static structure factors at the two temperatures, $T = 0.75$ and 3.0, are shown in Fig. 1. Both functions exhibit a strong peak at $q = 6.8$, which represents the correlation between adjacent molecules. At the higher temperature, the peak height was lower and the peak was broader, which can be ascribed to the increased thermal fluctuation and the decrease in the effective size of the molecules due to the softness of the repulsive core. At wavenumbers lower than the peak, the structure factors were small, representing small isothermal compressibility. All the above properties are typical for dense liquids.

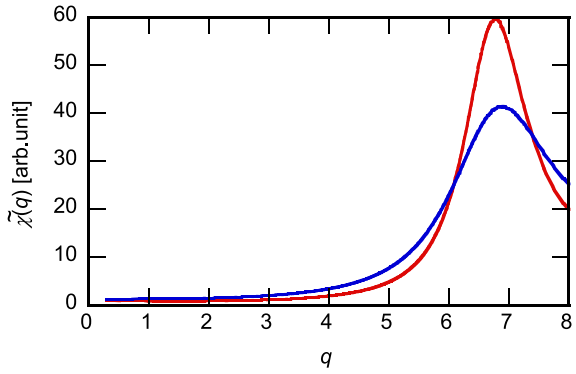

FIG. 1. The static structure factors of the LJ fluids at $T = 0.75$ (red) and 3.0 (blue).

The intermediate scattering functions were calculated at wavenumbers $q = nq_{\mathrm{min}}$, where n is an integer, and $q_{\mathrm{min}} = \frac{2\pi}{L} = 0.298$ was the smallest wavenumber of the cubic cell of the size L. The intermediate scattering functions at $T = 0.75$ and at the four lowest wavenumbers are plotted in Fig. 2. The functions at these wavenumbers clearly showed damped oscillation, and both the frequency and the damping of the oscillation became faster with increasing q. The results of the MD simulation were, then, fitted by Eq. (13); $\tilde{\chi}(q)$, $a_P(q)$, $k_T(q)$, $\omega_P'(q)$, and $k_P(q)$ were treated as fitting parameters. The fitting functions describe the simulation results well (Fig. 2).

The wavenumber-dependent sound velocities, $c(q)$, determined from the fitting, are shown in Fig. 3. The low- and high-frequency limiting values of the isothermal and the adiabatic sound velocities were also calculated from Eqs. (15), (16), (18) and (19) and were plotted together for comparison. The results at $T = 0.75$ and 3.0 are shown separately in Figs. 3(a) and 3(b), respectively.

The sound velocity increases with q in the low-q regime at both temperatures. It exhibits a maximum at an intermediate q and then decreases with q in the higher-q regime. The sound

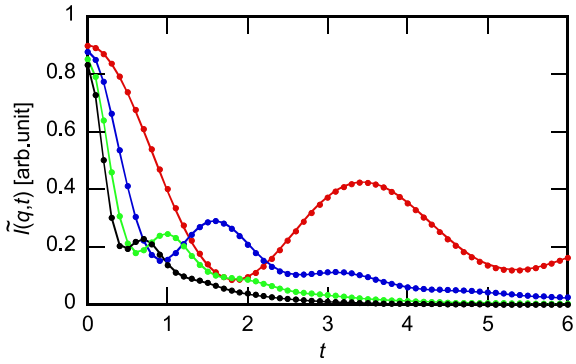

FIG. 2. The intermediate scattering functions at $T = 0.75$ and at wavenumbers $q = 0.298$ (red), 0.595 (blue), 0.892 (green), and 1.19 (black). The results of the MD simulation are shown with the filled circles, and the fitting curves from Eq. (13) are drawn with the solid curves.

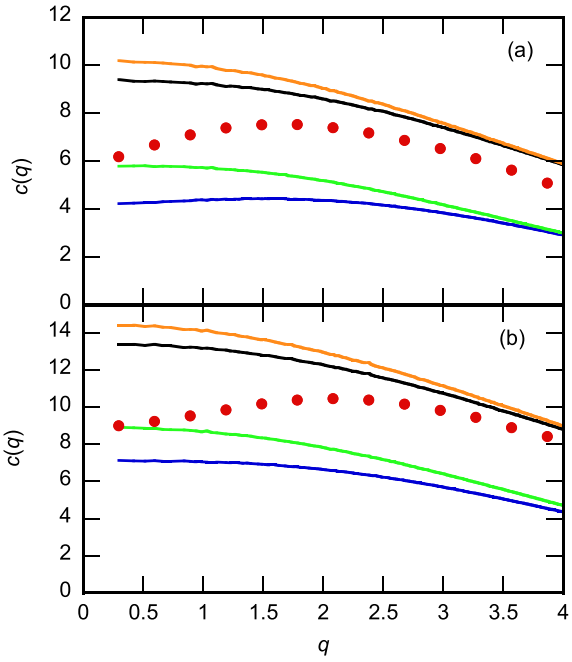

FIG. 3. The sound velocity as a function of wavenumber at the temperatures (a) $T = 0.75$ and (b) 3.0. The sound velocity determined from the fitting of the intermediate scattering functions is shown with the red circles, and the blue, green, black, and orange curves show $c_{T,0}(q)$, $c_{S,0}(q)$, $c_{T,\infty}(q)$, and $c_{S,\infty}(q)$, respectively.

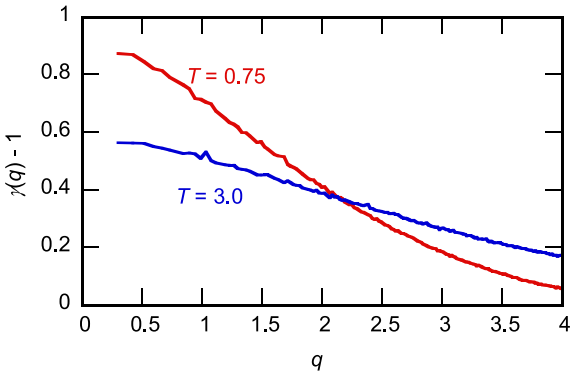

FIG. 4. The heat capacity ratio as a function of the wavenumber. The values of $\gamma(q) - 1$ at $T = 0.75$ and 3.0 are plotted with the red and the blue curves, respectively.

velocity approaches $c_{S,0}(q)$ in the low-q limit. All these tendencies were already reported in literature studies.[9,12,13,15] Comparing the results at the two temperatures, the absolute value of the sound velocity increases with temperature, which is, of course, ascribed to the increased thermal velocity of the molecules. In addition, the approach of $c(q)$ to $c_{S,0}(q)$ occurs at higher q, which can be understood as the faster viscoelastic relaxation at the higher temperature.

The sound velocity exhibits a maximum at $q = 1.8$ at $T = 0.75$ and at $q = 2.1$ at $T = 3.0$, and it displays a plateau around the maximum wavenumber. However, compared with the high-frequency limiting values, $c_{T,\infty}(q)$ and $c_{S,\infty}(q)$, the plateau never means that the high-frequency limiting behavior was reached. Rather, the plateau is realized as the result of the competition of the increasing trend at lower-q and the decreasing one at higher-q. The former is ascribed to the viscoelastic relaxation, and the latter is ascribed to the softening of the static structure factor of Eq. (15).

Another point to be noted is that the difference between $c_{T,0}(q)$ and $c_{S,0}(q)$ decreases with increasing q. Given that the ratio of their squares defines the heat capacity ratio through Eq. (17), their decrease in difference means the decrease in $\gamma(q)$ with q. The values of $\gamma(q) - 1$ at both temperatures calculated from Eq. (17) are plotted in Fig. 4 as a function of the wavenumber. A decrease with q is observed at both temperatures, as expected, and the degree of decrease is larger at the lower temperature. Although $\gamma(q)$ around $q = 0$ is larger at the lower temperature, the order is inverted at higher q.

As $\gamma(q)$ in the hydrodynamic limit is the thermodynamic quantity given by the ratio of the isobaric and isochoric heat capacities, the decrease in $\gamma(q)$ with q requires some explanation. According to Eq. (6), the expression of $c_{S,0}(q)$ involves the time derivative of the momentum density, which becomes the pressure tensor in the $q = 0$ limit. The effect of the long-range attractive interaction on pressure is known to be larger than that of energy. Therefore, the attractive interaction may also contribute to the pressure tensor in the lower-q regime, and its contribution can decrease with q due to the long-range nature of the attractive interaction. The contribution of the attractive interaction naturally decreases with temperature. We, thus, consider that the dispersion of $\gamma(q)$ in Fig. 4 originates from the intermolecular attractive interaction.

According to Eq. (23), the frequency-dependent longitudinal modulus, $\Delta G_L'(q,\omega)$, can be estimated from the sound velocity dispersion as follows:

$$\Delta G_L'(q, \omega_P(q)) = \rho_m \left[c^2(q) - c_{S,0}^2(q)\right]. \tag{43}$$

Similarly, based on Eqs. (20) and (24), the longitudinal viscosity, $\eta_L'(q, \omega_P(q))$, is also evaluated from the fitting parameters of the intermediate scattering functions as follows:

$$\eta_L'(q, \omega_P(q)) = \frac{\rho_m}{q^2}\left[2k_P(q) - [\gamma(q) - 1]k_T(q)\right]. \tag{44}$$

Both of these equations contain the information on the physical properties at the finite wavenumber. By contrast, their $q = 0$ counterparts can be calculated from the time correlation functions of the shear stress or the adiabatic pressure fluctuation through Eqs. (25)–(29). Their comparison tells us whether we need to take the q-dependence of the physical properties into account in the analysis of Brillouin spectroscopy on the molecular scale.

The comparison between the longitudinal modulus from the intermediate scattering function (filled circles) and that from the Kubo–Green theory (solid curve) is performed in Fig. 5(a), where they agree well with each other at both temperatures at $q < 2$. This seems to suggest that the q-dependence of the physical properties is unnecessary for the sound dispersion description up to $q = 2$, and the fast sound of the LJ fluid is wholly ascribed to the longitudinal viscoelastic relaxation. However, it should be kept in mind that here we

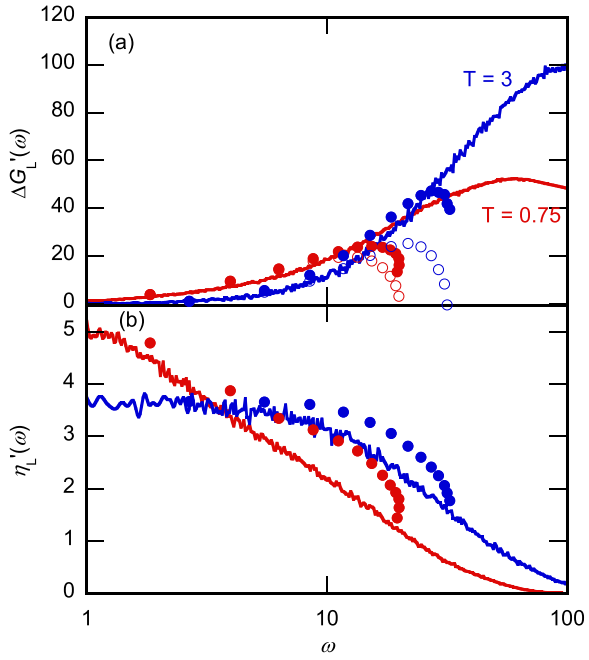

FIG. 5. (a) The longitudinal modulus, $\Delta G_L'(\omega)$, and (b) the longitudinal viscosity, $\eta_L'(\omega)$, as functions of frequency. The results at $T = 0.75$ and 3.0 are shown with the red and the blue symbols, respectively. The functions from the intermediate scattering function are shown with the filled circles, and the results from the Kubo–Green theory are shown with the solid curves. In (a), the open circles show the results of Eq. (43) when replacing $c_{S,0}(q)$ with the results at the lowest wavenumber, $q_{min} = 0.298$.

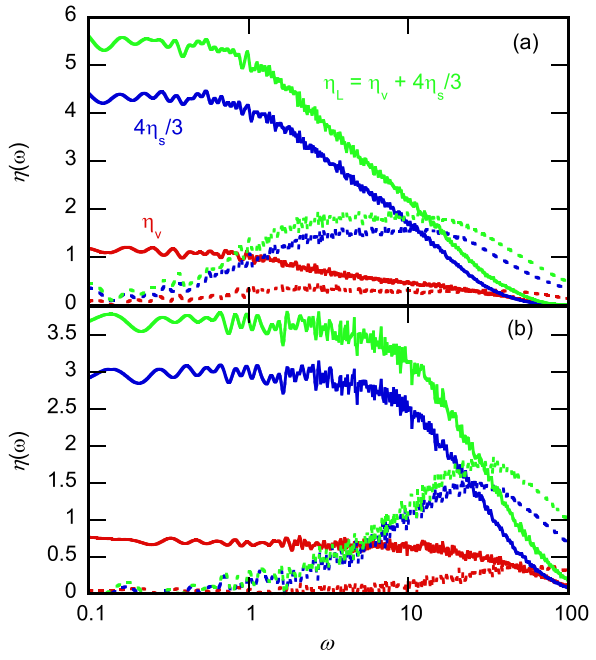

FIG. 6. The viscoelastic relaxation as a function of frequency at the temperatures of (a) $T = 0.75$ and (b) 3.0. The longitudinal complex viscosity (green) is divided into the contributions of shear (blue) and volume (red) viscosities. The real and the imaginary parts are drawn with the solid and the dotted curves, respectively.

used the information on the q-dependence of $c_{S,0}(q)$, which was not available in the experiment. Because experimental analysis is usually performed based on the comparison between $c(q)$ and $c_{S,0}(q \simeq 0)$, we also calculated $\Delta G_L'(q,\omega)$ using Eq. (43) replacing $c_{S,0}(q)$ with the constant value at the lowest wavenumber, $q_{min} = 0.298$ (open circles). The replacement makes the deviation of $\Delta G_L'(q,\omega)$ from $\Delta G_L'(\omega)$ faster, indicating that the information on the q-dispersion of heat capacity ratio is necessary for the quantitative analysis of the fast sound in the higher-q regime.

The corresponding comparison on the longitudinal viscosity is shown in Fig. 5(b). Although the value of $\eta_L'(q,\omega)$ from the intermediate scattering function was close to that of $\eta_L'(\omega)$ from the Kubo–Green theory, they did not agree as well as the longitudinal modulus. The agreement is quantitatively good at the lowest wavenumber, $q_{min} = 0.298$, at both temperatures, but the estimation from the intermediate scattering function overestimates the longitudinal viscosity at higher wavenumbers.

The fast sound of the LJ fluids is explained by the longitudinal viscoelastic relaxation, $\eta_L(\omega)$, which, in turn, is given by the linear combination of the shear and the volume viscosities according to Eq. (9). It is, thus, interesting to determine which component is more important in sound dispersion, $\eta_s(\omega)$ or $\eta_v(\omega)$. In Fig. 6, the complex longitudinal viscosity, $\eta_L(\omega)$, is divided into the contributions of the shear and the volume viscosities at both temperatures. The real and the imaginary parts are plotted together, and the latter corresponds to the longitudinal modulus according to Eq. (22).

In Fig. 6(a), the viscoelastic relaxation at $T = 0.75$ is clearly bimodal, as in the cases of dense liquids. The faster and the slower relaxation modes are usually assigned to binary collision and structural relaxation, respectively. The latter relaxation mode disappears at $T = 3.0$, which makes the overall viscoelastic relaxation to be faster. As discussed in relation to the sound dispersion in Fig. 3, the faster deviation of $c(q)$ from $c_{S,0}(q)$ at the lower temperature is ascribed to the slower viscoelastic relaxation of Fig. 6. Comparing the contributions of $\eta_s(\omega)$ and $\eta_v(\omega)$, the former is dominant in $\eta_L(\omega)$ at both temperatures. Therefore, it is safe to say that the fast sound of LJ fluids is caused mainly by shear relaxation. Bolmatov and co-workers studied the collective dynamics of compressed argon by both inelastic x-ray scattering and MD simulation.[15] They found that the emergence of the transverse wave is correlated with that of the fast sound and concluded that the fast sound is caused by the shear part of the viscoelastic relaxation. The dominance of the shear contribution to the longitudinal viscoelastic relaxation (Fig. 6) is, thus, in harmony with their conclusion.

A comment regarding the deviation between $\eta_L'(q,\omega)$ from the intermediate scattering function and $\eta_L'(\omega)$ from the Kubo–Green theory is as follows: in the calculation, it was assumed that the rate of exponential decay of the intermediate scattering function is governed by the heat diffusivity [Eq. (20), which was used in transforming Eq. (24) into Eq. (44)]. The decay of the energy density is also governed by heat diffusion, and $\tilde{\rho}_n(q)$ and $\tilde{\rho}_{e'}(q)$ were expected

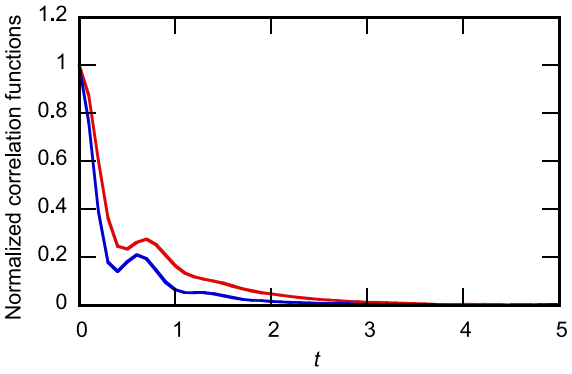

FIG. 7. The normalized autocorrelation functions of $\tilde{\rho}_{\mathrm{n}}(q)$ (red) and $\tilde{\rho}_{\epsilon'}(q)$ (blue) at $T = 0.75$ and $q = 1.19$.

according to Eq. (20) to decay at the same rate. The normalized autocorrelation functions of $\tilde{\rho}_{\mathrm{n}}(q)$ and $\tilde{\rho}_{\epsilon'}(q)$ at $T = 0.75$ and $q = 1.19$ are shown in Fig. 7. Both correlation functions consist of fast oscillation and slow decay. Comparing their slow relaxation, the decay of $\tilde{\rho}_{\epsilon'}(q)$ appears to be a little faster than that of $\tilde{\rho}_{\mathrm{n}}(q)$. This suggests that the dynamics of the energy density is partly decoupled from that of the number density at this wavenumber, which violates one of the assumptions in the derivation of Eq. (44). We believe that this might be one of the reasons for the deviation in longitudinal viscosity observed in Fig. 5(b).

B. Rigid cyclohexane in chair conformation

The static structure factor of this cyclohexane model is shown in Fig. 8. The structure factor presents a strong peak at $q = 12.5\ \mathrm{nm}^{-1}$, and the whole shape of the structure factor resembles the simple LJ fluid (Fig. 1). The self-part of the static structure factor was calculated by taking only the intramolecular correlation into account and was also added to the plot. The self-part is a monotonically decreasing function of q, and the peak width around $q = 0$ indicates the reciprocal size of the spatial distribution of the sites within a molecule.

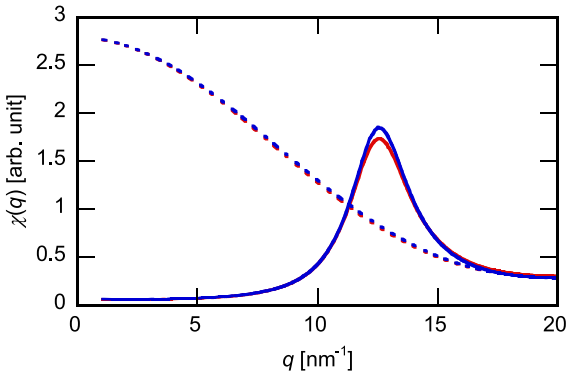

FIG. 8. The static structure factor (solid curves) of the liquid cyclohexane model and its self-part (dotted curves). The functions for the rigid and flexible models are drawn in red and blue, respectively.

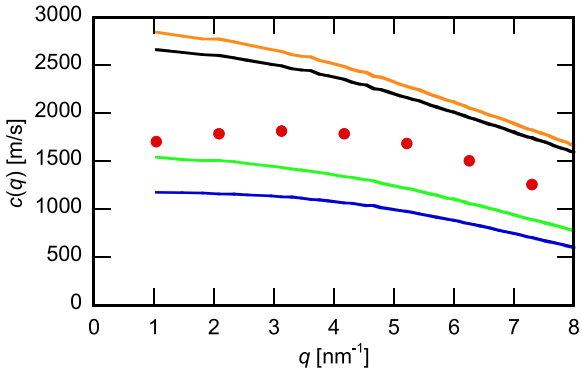

FIG. 9. The sound velocity of rigid cyclohexane as a function of wavenumber. The sound velocities determined from the fitting of the intermediate scattering functions are shown with the red circles, and the blue, green, black, and orange curves show $c_{\mathrm{T},0}(q)$, $c_{\mathrm{S},0}(q)$, $c_{\mathrm{T},\infty}(q)$, and $c_{\mathrm{S},\infty}(q)$, respectively.

The intermediate scattering function was calculated at wavenumbers $q = nq_{\mathrm{min}}$, where $q_{\mathrm{min}} = 1.04\ \mathrm{nm}^{-1}$ is the minimum wavenumber of the cubic cell, and it was fitted into Eq. (13) to obtain necessary parameters. The wavenumber-dependent sound velocity determined from the intermediate scattering function, $c(q)$, is shown in Fig. 9 as a function of q, together with $c_{\mathrm{T},0}(q)$, $c_{\mathrm{S},0}(q)$, $c_{\mathrm{T},\infty}(q)$, and $c_{\mathrm{S},\infty}(q)$ calculated from the static correlation functions.

The wavenumber dependence of the sound velocity of rigid cyclohexane liquid resembles that of the simple LJ fluid (Fig. 3). The sound velocity from the intermediate scattering function, $c(q)$, is always larger than $c_{\mathrm{T},0}(q)$ and $c_{\mathrm{S},0}(q)$. A plateau is observed around $q = 3$–$4\ \mathrm{nm}^{-1}$ in $c(q)$, and it decreases with decreasing q to approach $c_{\mathrm{S},0}(q)$ at the $q = 0$ limit. The decrease in $c(q)$ with increasing q at $q > 5\ \mathrm{nm}^{-1}$ is ascribed to the decreases in $c_{\mathrm{T},0}(q)$ and $c_{\mathrm{S},0}(q)$. The difference between $c_{\mathrm{T},0}(q)$ and $c_{\mathrm{S},0}(q)$ decreases with q, suggesting the wavenumber dependence of the heat capacity ratio.

The heat capacity ratio is plotted in Fig. 10 as a function of the wavenumber q. The value of $\gamma(q)$ around $q = 0$ is as large as those of the LJ fluids of Fig. 4, and it decreases with increasing q, as also observed in the LJ fluids. Compared with the LJ fluids, however, the decrease is smaller, and an increase is observed in the higher q

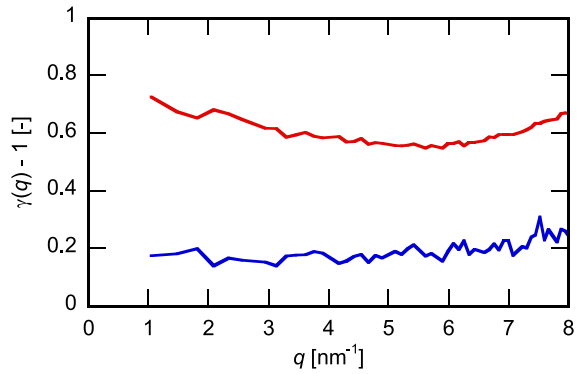

FIG. 10. The heat capacity ratio of liquid cyclohexane as a function of the wavenumber in the rigid (red) and the flexible (blue) models.

regime. The origins of the difference were not explored in this work, but there are many possible reasons, as follows: First is the contribution of the rotational energy to the heat capacity ratio; second is the finite size of the molecule; and third is that the range of the attractive interaction is relatively small in molecular liquids because it is determined by the size of the interaction site rather than that of the whole molecule.

The longitudinal modulus and longitudinal viscosity were calculated from the intermediate scattering function using Eqs. (43) and (44), respectively, and compared with those of the $q = 0$ limit from the Kubo–Green theory in Fig. 11. The agreement with the longitudinal modulus [Fig. 11(a)] covers up to $q = 4$ nm^{-1} [the range for which the dependence of $c_{S,0}(q)$ on the wavenumber is included in Eq. (43)]. The deviation appears at lower q values, $q \cong 2$–3 nm^{-1}, when $c_{S,0}(q)$ is replaced with $c_{S,0}(q_{min})$. The agreement for the longitudinal viscosity [Fig. 11(b)] is worse than that for the longitudinal modulus [Fig. 11(a)]. Although good agreement is observed at $q = q_{min}$, the longitudinal viscosity from the intermediate scattering function is larger than that of the Kubo–Green theory at higher q. The longitudinal viscosity in Fig. 11(b) exhibits a bimodal relaxation, with the faster and the slower modes at around 0.5 and 20 ps^{-1}, respectively. The bimodal relaxation resembles that of the LJ liquid at $T = 0.75$, and the two relaxation modes can be assigned to the structural relaxation and the binary collision, respectively. The frequency range of the sound dispersion calculated in the present MD simulation, $1 < \omega < 10$ ps^{-1}, was higher than that of the structural relaxation, and hence, the structural relaxation is frozen in the fast sound observed in this work.

The complex frequency-dependent longitudinal viscosity is divided into the contributions of the shear and volume viscosities in Fig. 12. Bimodal relaxation is observed in both $\eta_s(\omega)$ and $\eta_v(\omega)$, and the relaxation frequencies of both modes of $\eta_v(\omega)$ are a little higher than those of $\eta_s(\omega)$. The contribution of the shear viscosity amounts to about two-thirds of the longitudinal viscosity, which means that the fast sound in this model cyclohexane was mainly caused by shear relaxation. Compared with the results of monoatomic LJ fluids (Fig. 6), the relative contribution of the volume viscosity was higher in the molecular liquid, which might be ascribed to the contribution of the rotational degrees of freedom.

In summary, the fast sound was observed in the liquid cyclohexane of the rigid model and was ascribed to the longitudinal viscoelastic relaxation. The longitudinal modulus calculated from the sound dispersion agreed well with that at the $q = 0$ limit of the Kubo–Green theory up to $q = 4$ nm^{-1}, when the wavenumber-dependence of $c_{S,0}(q)$ is taken into account; the replacement of $c_{S,0}(q)$ with $c_{S,0}(q_{min})$ lowers the wavenumber, at which stage the deviation from the $q = 0$ spectrum begins. The longitudinal viscosity originates mainly from the shear viscosity, although the contribution of the volume viscosity is not negligible. All the properties above are qualitatively similar to those of the monoatomic LJ fluids, and we consider that the sound dispersion of the rigid polyatomic liquid shares the common mechanism to that of the simple liquid.

C. Flexible cyclohexane

The static structure factor of the flexible cyclohexane liquid and its self-part are plotted in Fig. 8 together with those of the rigid model. They show that the liquid structure is almost the same irrespective of the intramolecular constraint. Small differences were found in both functions, and these may be ascribed to the distortion of the intramolecular structure by the intermolecular interaction and the minor but non-negligible population of the boat conformation in the flexible model.

The sound velocity was calculated from the intermediate scattering function through the fitting by Eq. (13) and was compared

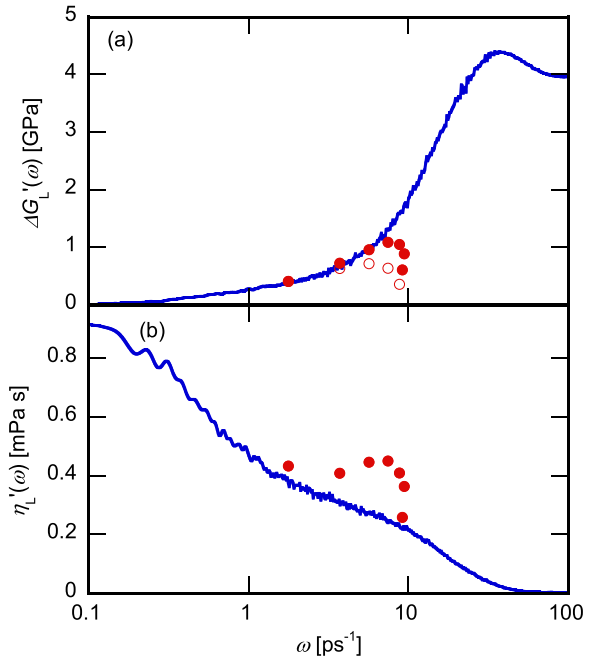

FIG. 11. (a) The longitudinal modulus as a function of frequency, $\Delta G_L'(\omega)$, and (b) the longitudinal viscosity of liquid cyclohexane in the rigid model as a function of frequency. The functions from the intermediate scattering function are shown with the red filled circles, and those from the Kubo–Green theory are shown with the blue solid curves. The open circles in (a) represent the results of Eq. (43) with replacing $c_{S,0}(q)$ by the results at the lowest wavenumber, $q_{min} = 1.04$ nm^{-1}.

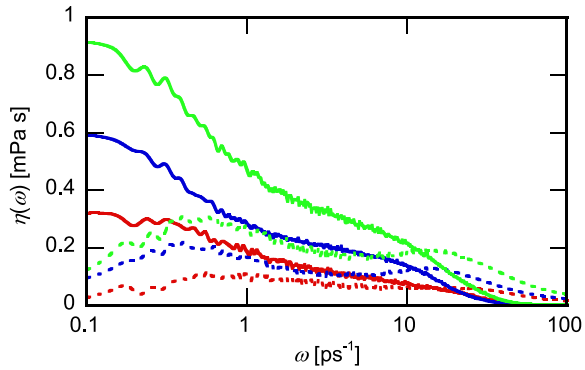

FIG. 12. The viscoelastic relaxation of rigid cyclohexane liquid. The complex longitudinal viscosity (green) is composed of the contributions of the shear (blue) and volume (red) viscosities. The real and imaginary parts are drawn with the solid and the dotted curves, respectively.

with the low-frequency limits of the isothermal and adiabatic sound velocities, $c_{T,0}(q)$ and $c_{S,0}(q)$ (Fig. 13). The high-frequency limits $c_{T,\infty}(q)$ and $c_{S,\infty}(q)$ are not shown here because they are extremely high due to the intramolecular vibration. The corresponding results on the rigid model, which were already shown in Fig. 9, are plotted together for comparison.

The sound velocity from the intermediate scattering function is almost independent of the treatment of the intramolecular degrees of freedom. The difference in the low-frequency isothermal sound velocity is also small, reflecting the similarity of the static structure factor (Fig. 8). By contrast, the presence of the intramolecular degrees of freedom significantly reduces $c_{S,0}(q)$, particularly in the low-q region, $q < 5$ nm^{-1}. Due to the decrease in $c_{S,0}(q)$ in the flexible model, a large difference remains between $c(q)$ and $c_{S,0}(q)$ even at the lowest wavenumber of the present calculation, $q_{min} = 1.04$ nm^{-1}. Therefore, the degree of the fast sound compared with the hydrodynamic limit was large in the flexible model, and the large dispersion of the sound velocity was expected in the wavenumber regime lower than q_{min}.

Experimental results of Brillouin spectroscopy in the GHz frequency regime showed that a large dispersion of the sound velocity is observed in many organic liquids, including cyclohexane, and they are assigned to the vibrational energy relaxation.[18] Because the fluctuation of the intramolecular vibrational energy was fully included in the calculation of $c_{S,0}(q)$ using Eq. (16), it is regarded as the low-frequency limiting value of the sound dispersion due to the vibrational energy relaxation. By contrast, the frequency of the sound in this wavenumber regime is of the order of THz, which is much higher than the frequency of vibrational energy relaxation reported in experimental works. Therefore, it is plausible that a large sound dispersion is present at $q < q_{min}$ due to the vibrational energy relaxation.

The wavenumber-dependent heat capacity ratio defined by the ratio of $c^2_{S,0}(q)$ to $c^2_{T,0}(q)$ is plotted in Fig. 10 and is compared with that of the rigid model. The presence of intramolecular degrees of freedom significantly reduces the heat capacity ratio, as is expected from Fig. 13, and the wavenumber dependence of $\gamma(q)$ also becomes weaker. The decrease in the heat capacity ratio at the $q = 0$ limit can also be understood in terms of thermodynamic heat capacity. Because the intramolecular vibrational heat capacity contributes almost equally to the isobaric and isochoric heat capacities, its inclusion naturally reduces the ratio of the two heat capacities. However, the vibrational heat capacity is overestimated in the present classical MD simulation, which leads to the underestimation of $\gamma(q)$ in the flexible model.

The longitudinal modulus and the longitudinal viscosity were calculated from the intermediate scattering functions and were compared with those at $q = 0$ evaluated by the Kubo–Green theory in Fig. 14. In Fig. 14, the longitudinal modulus exhibits a nonzero offset near $\omega = 0.1$ ps^{-1}, and the longitudinal viscosity increases with the decreasing frequency in the same frequency range. These offsets and increases originate from the relaxation mode in the lower frequency regime. The oscillatory behavior near $\omega = 100$ ps^{-1} is due to the intramolecular vibration.

According to Fig. 14(a), the longitudinal modulus from the intermediate scattering function is described by the modulus at $q = 0$ up to $q = 3$ nm^{-1}. Therefore, the fast sound at $q \lesssim 3$ nm^{-1} is explained by the viscoelastic relaxation at the low-q limit. Although the results of the replacement are not shown for brevity, the neglect of the q-dependence of $c_{S,0}(q)$ hardly affects this conclusion because the variation of $c_{S,0}(q)$ is small at $q \lesssim 3$ nm^{-1}, as shown in Fig. 13. The agreement in the longitudinal viscosity is not so good compared with that in the longitudinal modulus, as are the cases of the LJ fluid and the rigid cyclohexane.

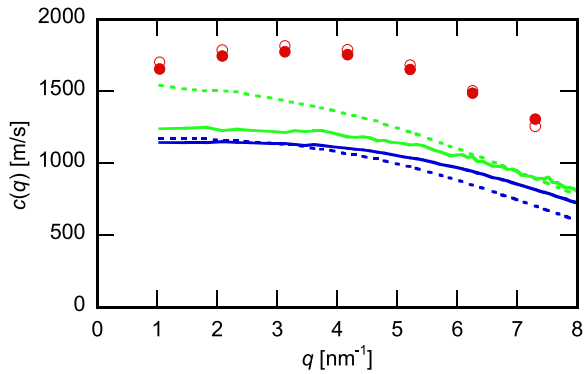

FIG. 13. The sound velocity of liquid cyclohexane as a function of the wavenumber. The sound velocity determined from the fitting of the intermediate scattering functions is shown with the red circles, and the blue and green curves show $c_{T,0}(q)$ and $c_{S,0}(q)$, respectively. The results of the flexible model are shown with the filled or solid symbols, and those of the rigid model are shown with the open or dotted ones.

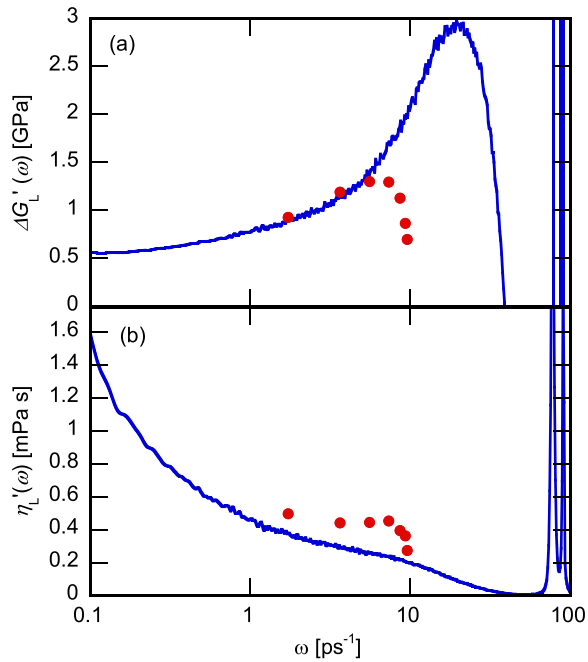

FIG. 14. (a) The longitudinal modulus, $\Delta G_L'(\omega)$, as a function of frequency and (b) the longitudinal viscosity, $\eta_L'(\omega)$, of liquid cyclohexane in the flexible model as functions of frequency. The functions from the intermediate scattering function are shown with the red filled circles; the blue solid curves follow the function of the Kubo–Green theory.

The longitudinal modulus at $q = 0$ shown in Fig. 14(a) is divided into the contributions of the shear and the volume moduli according to Eq. (9). The latter is, then, further divided into the rigid and the intramolecular parts based on the theoretical formalism described in Sec. II C. The division was numerically performed on flexible cyclohexane, and the results are shown in Fig. 15. The contributions of the shear and the volume moduli to the longitudinal modulus of rigid cyclohexane are also plotted together for comparison.

The contribution of the intramolecular vibration is nearly constant at $\omega < 10$ ps^{-1}, which describes the excess modulus when the intramolecular vibrational energy is frozen. Since the longitudinal viscosity converges to the constant value at $\omega = 0.1$ ps^{-1}, the offset of the longitudinal modulus is assigned to the vibrational energy relaxation. Both the shear and the rigid parts are close to zero at $\omega = 0.1$ ps^{-1}, and they increase with the increasing frequency of up to 10 ps^{-1}. Therefore, the relaxation processes other than the intramolecular mode are completed at $\omega < 0.1$ ps^{-1}. Provided that the sound dispersion at $q \leq 3$ nm^{-1} corresponds to the longitudinal modulus at $q = 0$, $c(q)$ at $q < q_{\min}$ is expected to converge to the high-frequency limiting value of the vibrational energy relaxation with decreasing q.

The frequency-dependent shear and volume moduli of the rigid cyclohexane are also plotted in Fig. 15, which are close to the shear and rigid parts of the flexible model at $\omega < 10$ ps^{-1}. It can be naturally understood as that the intramolecular vibrational modes behave as frozen at frequencies higher than the vibrational energy relaxation; this is also in harmony with the sound dispersion in Fig. 13, which showed that $c(q)$ is hardly affected by the introduction of intramolecular constraints. Therefore, the difference in acoustic properties of these two models is that the presence of the intramolecular vibrational modes lowers the heat capacity ratio through the vibrational heat capacity at frequencies lower than the vibrational energy relaxation, which decreases $c_{S,0}(q)$ and increases the apparent degree of the fast sound.

The time correlation function of $\delta E_2'(t)$ is plotted in Fig. 16 to show the time scale of vibrational energy relaxation. The correlation function is divided by the number of molecules, N. The vibrational energy relaxation hardly occurs up to several ps, which is in harmony with the constant $\omega\eta_{v2}''(\omega)$ (green curve) in Fig. 15. The time correlation function decays on the time scale of 100 ps, and the decay is almost completed at $t = 5$ ns.

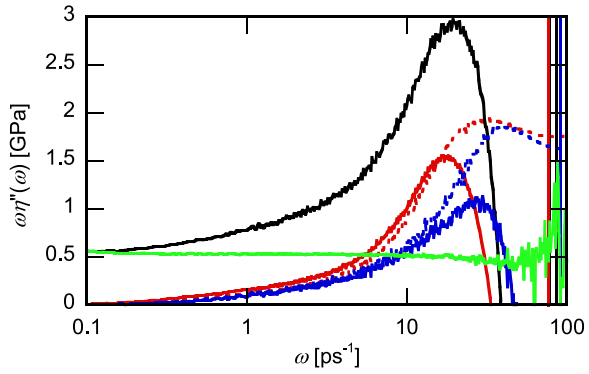

FIG. 15. The longitudinal modulus of the flexible cyclohexane at the $q = 0$ limit (black solid curve) is divided into the shear modulus (red solid curve), the rigid part (blue solid curve), and the intramolecular part (green solid curve) of the volume modulus, $\omega\eta_v''(\omega)$. The corresponding functions of the rigid model $\omega\eta_s''(\omega)$ (red dotted) and $\omega\eta_v''(\omega)$ (blue dotted) are plotted together for comparison.

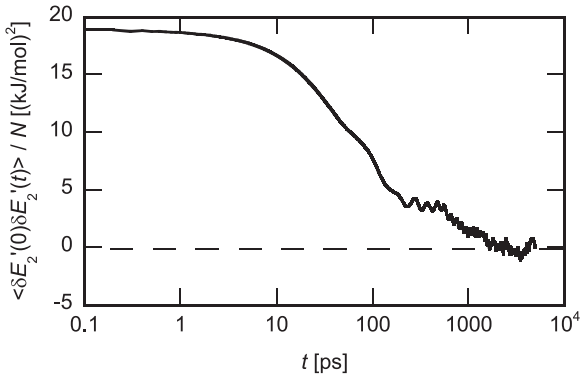

FIG. 16. The time correlation function of $\delta E_2'(t)$.

The energy relaxation due to the intramolecular conformational isomerization is included in the vibrational energy relaxation in the present definition, in addition to the relaxation of the intramolecular vibrational mode around the energy minimum of each conformation. The relaxation of the conformational equilibrium is, thus, buried within the decay of the correlation function in Fig. 16, and its contribution is not separated. Campbell and co-workers determined the rate of the conformational isomerization of liquid cyclohexane as the function of pressure using nuclear magnetic resonance spectroscopy.[30] They found that the isomerization rate is an increasing function of pressure, which means that the isomerization reaction rate is limited by the activation of the intramolecular vibrational energy. If the same mechanism also holds for our model system, the time scale of the conformational isomerization is expected to be similar to or longer than the vibrational energy relaxation. A rough analysis of the chair–boat conformational isomerization is performed in Sec. S2 of the supplementary material, which shows that the equilibration rate of the isomerization reaction is about 2×10^9 s^{-1}. Anyway, it is safely said that the conformational isomerization is also frozen within the time scale of acoustic oscillation.

The decoupling between the acoustic dynamics and the intramolecular vibrational energy can also be confirmed from the dynamics of $\tilde{\rho}_n(\boldsymbol{q})$, $\tilde{\rho}_{\epsilon 1'}(\boldsymbol{q})$, and $\tilde{\rho}_{\epsilon 2'}(\boldsymbol{q})$. Their time correlation functions at $q = q_{\min}$ are normalized and plotted in Fig. 17. The normalization factors of the autocorrelation functions are their initial values, and those of the cross-correlation functions are the geometric means of the initial values of the autocorrelation functions of the corresponding components.

The autocorrelation functions of both $\tilde{\rho}_n(\boldsymbol{q})$ and $\tilde{\rho}_{\epsilon 1'}(\boldsymbol{q})$ are composed of acoustic oscillation and the slow exponential decay, as is represented in Eq. (13). Their cross-correlation function is negative, and they oscillate with the same frequency, which indicates that $\tilde{\rho}_n(\boldsymbol{q})$ and $\tilde{\rho}_{\epsilon 1'}(\boldsymbol{q})$ are coupled with each other through the adiabatic compression of the sound wave. By contrast, the autocorrelation function of $\tilde{\rho}_{\epsilon 2'}(\boldsymbol{q})$ shows a quite fast oscillation and very slow

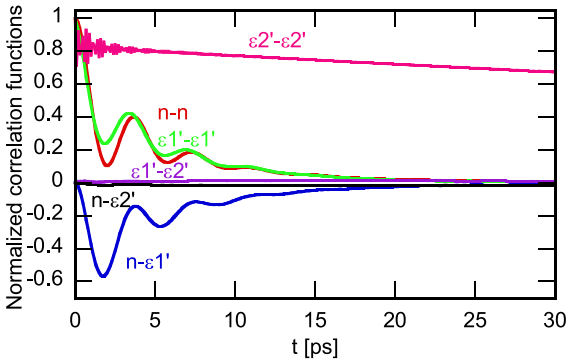

FIG. 17. The normalized time correlation functions associated with $\tilde{\rho}_n(\boldsymbol{q})$, $\tilde{\rho}_{\epsilon 1'}(\boldsymbol{q})$, and $\tilde{\rho}_{\epsilon 2'}(\boldsymbol{q})$ of flexible cyclohexane at $q = q_{\min}$.

decay. The former corresponds to the intramolecular vibration, and the latter corresponds to the vibrational energy relaxation and the diffusion of vibrationally hot molecules. The decay rate of the slow component, thus, indicates that the vibrational energy relaxation is slower than the oscillation of the sound wave. The acoustic oscillation does not appear in the correlation functions involving $\tilde{\rho}_{\epsilon 2'}(\boldsymbol{q})$, and the cross correlations with $\tilde{\rho}_n(\boldsymbol{q})$ and $\tilde{\rho}_{\epsilon 1'}(\boldsymbol{q})$ are almost zero, which means that the intramolecular vibrational energy density is decoupled from the sound wave. Although the adiabatic compression of the sound wave increases the translational and the rotational energies, they are not transferred into the intramolecular vibrational energy during the period of the acoustic oscillation.

Kamiyama and co-workers performed an experiment on inelastic x-ray scattering of liquid CCl_4.[6] They determined the sound dispersion in the nm^{-1} regime and compared it with the sound velocity in the GHz regime that exhibits a dispersion due to the vibrational energy relaxation. By fitting the dispersion in the nm^{-1} regime into a model function, they concluded that the sound dispersion in the nm^{-1} regime is connected to the low-frequency limit of the vibrational energy relaxation, rather than the high-frequency limit. Their conclusion appears to disagree with our present result that the intramolecular vibrational energy is frozen during the acoustic oscillation in the nm^{-1} regime. A possible explanation for the disagreement is that the wavenumber-dependent heat capacity ratio was not taken into account in their experimental analysis, which leads to an underestimation of the excess longitudinal modulus caused by the viscoelastic relaxation.

VI. SUMMARY

In this work, the sound dispersion of three molecular liquids in the molecular scale wavenumber range was studied by MD simulation. A sound velocity faster than the hydrodynamic limit was observed in all the systems, and it was explained by the longitudinal viscoelastic relaxation. The comparison with the frequency-dependent longitudinal modulus at the $q = 0$ limit, which was evaluated by the Kubo–Green theory, showed that the fast sound up to $q \sim 2$ nm^{-1} can be explained quantitatively by the longitudinal modulus in the $q = 0$ limit, indicating that the emergence of the fast sound is ascribed to the longitudinal viscoelastic relaxation. The heat capacity ratio and, thus, the adiabatic sound velocity in the low-frequency limit exhibit a q-dependence in the higher-q regime, which should be taken into account for the quantitative analysis of the sound dispersion in this wavenumber regime.

The consideration of the intramolecular vibrational degrees of freedom decreases the adiabatic sound velocity in the low-frequency limit, whereas the sound dispersion in the nm^{-1} range is hardly affected by the intramolecular vibration. This means that the intramolecular modes behave as frozen at a frequency higher than the vibrational energy relaxation. The degree of fast sound is, thus, increased by the intramolecular vibrational degrees of freedom. The vibrational energy relaxation also appears in the longitudinal viscoelastic relaxation at the $q = 0$ limit, and the longitudinal modulus in the $q = 0$ limit quantitatively describes the sound dispersion up to 2–3 nm^{-1} even in the presence of the vibrational energy relaxation. A theoretical formulation to extract the contribution of the vibrational energy relaxation in the viscoelastic relaxation was proposed based on the projection operator formalism. After subtracting the contribution of the vibrational energy relaxation thus determined, the remaining viscoelastic relaxation agrees well with that of the rigid molecular model without intramolecular degrees of freedom.

We recently measured the sound dispersion of some molecular liquids, including cyclohexane, in the nm^{-1} range by means of the inelastic x-ray scattering method. An analysis based on the theoretical formalism proposed in this work is now in progress.

SUPPLEMENTARY MATERIAL

See the supplementary material for the derivation of Eq. (42) and an analysis of conformational isomerization of flexible cyclohexane.

ACKNOWLEDGMENTS

The author is grateful to Professor K. Yoshida (Fukuoka Univ.) and S. Hosokawa (Kumamoto Univ.) for discussions. This work was financially supported by the Japan Society for the Promotion of Science (JSPS) KAKENHI (Grant No. 19K03768).

AUTHOR DECLARATIONS

Conflict of Interest

The author has no conflicts to disclose.

Author Contributions

Tsuyoshi Yamaguchi: Conceptualization (equal); Data curation (equal); Formal analysis (equal); Funding acquisition (equal); Investigation (equal); Methodology (equal); Project administration (equal); Resources (equal); Software (equal); Supervision (equal); Validation (equal); Visualization (equal); Writing – original draft (equal); Writing – review & editing (equal).

DATA AVAILABILITY

The data that support the findings of this study are available from the corresponding author upon reasonable request.

REFERENCES

[1] U. Kaatze, T. O. Hushcha, and F. Eggers, J. Solution Chem. **29**, 299 (2000).
[2] F. Sette, G. Ruocco, M. Krisch, C. Masciovecchio, R. Verbeni, and U. Bergmann, Phys. Rev. Lett. **77**, 83 (1996).
[3] K. Fujii, M. Shibayama, T. Yamaguchi, K. Yoshida, T. Yamaguchi, S. Seki, H. Uchiyama, A. Q. R. Baron, and Y. Umebayashi, J. Chem. Phys. **138**, 151101 (2013).
[4] K. Yoshida, N. Yamamoto, S. Hosokawa, A. Q. R. Baron, and T. Yamaguchi, Chem. Phys. Lett. **440**, 210 (2007).
[5] K. Yoshida, N. Fukuyama, T. Yamaguchi, S. Hosokawa, H. Uchiyama, S. Tsutsui, and A. Q. R. Baron, Chem. Phys. Lett. **680**, 1 (2017).
[6] T. Kamiyama, S. Hosokawa, A. Q. R. Baron, S. Tsutsui, K. Yoshida, W.-C. Pilgrim, Y. Kiyanagi, and T. Yamaguchi, J. Phys. Soc. Jpn. **73**, 1615 (2004).
[7] A. Cunsolo, B. M. Leu, A. H. Said, and Y. Q. Cai, J. Chem. Phys. **134**, 184502 (2011).
[8] S. Hosokawa, T. Kamiyama, K. Yoshida, T. Yamaguchi, S. Tsutsui, and A. Q. R. Baron, J. Mol. Liq. **332**, 115825 (2021).
[9] J.-P. Boon and S. Yip, *Molecular Hydrodynamics* (Dover, New York, 1991).
[10] J.-P. Hansen and I. R. McDonald, *Theory of Simple Liquids*, 2nd ed. (Academic Press, London, 1986).
[11] S. Miura, Mol. Phys. **87**, 1405 (1996).
[12] I. M. de Schepper, J. C. van Rijs, A. A. van Well, P. Verkerk, L. A. de Graaf, and C. Bruin, Phys. Rev. A **29**, 1602 (1984).
[13] M. Sampoli, U. Bafile, E. Guarini, and F. Barocchi, Phys. Rev. Lett. **88**, 085502 (2002).
[14] S.-H. Chong, Phys. Rev. E **74**, 031205 (2006).
[15] D. Bolmatov, M. Zhernenkov, D. Zav'yalov, S. Stoupin, Y. Q. Cai, and A. Cunsolo, J. Phys. Chem. Lett. **6**, 3048 (2015).
[16] C. Y. Liao, S. H. Chen, and F. Sette, Phys. Rev. E **61**, 1518 (2000).
[17] U. Bafile, F. Barocchi, and E. Guarini, Condens. Matter Phys. **11**, 107 (2008).
[18] K. Takagi, in *Ions and Molecules in Solutions*, edited by N. Tanaka, H. Ohtaki, and R. Tamamushi (Elsevier, Amsterdam, 1983), pp. 183.
[19] D. Samios and T. Dorfmüller, Mol. Phys. **41**, 637 (2007).
[20] M. G. Martin and J. I. Siepmann, J. Phys. Chem. B **102**, 2569 (1998).
[21] A. P. Shchemelev, V. S. Samuilov, N. V. Golubeva, and O. G. Poddubskii, J. Eng. Phys. Thermophys. **94**, 509 (2021).
[22] D. Ishikawa and A. Q. R. Baron, J. Phys. Soc. Jpn. **90**, 083602 (2021).
[23] J. A. McLennan, Prog. Theor. Phys. **30**, 408 (1963).
[24] R. Zwanzig, Annu. Rev. Phys. Chem. **16**, 67 (1965).
[25] P. L. Palla, C. Pierleoni, and G. Ciccotti, Phys. Rev. E **78**, 021204 (2008).
[26] T. Yamaguchi, Phys. Chem. Chem. Phys. **24**, 12311 (2022).
[27] S.-H. Chong and F. Hirata, J. Chem. Phys. **111**, 3083 (1999).
[28] M. J. Abraham, T. Murtola, R. Schulz, S. Páll, J. C. Smith, B. Hess, and E. Lindahl, SoftwareX **1–2**, 19 (2015).
[29] M. P. Allen and D. J. Tildesley, *Computer Simulation of Liquids* (Clarendon Press, Oxford, 1987).
[30] D. M. Campbell, M. Mackowiak, and J. Jonas, J. Chem. Phys. **96**, 2717 (1992).